Electronic Supplementary Material (ESI) for Journal of Materials Chemistry A.

K^+, Ni and carbon co-modification promoted two-electron O_2 reduction for photocatalytic H_2O_2 production by crystalline carbon nitride

Yanfang Chen, Xuemei Yan, Jixiang Xu*, Lei Wang*

Key Laboratory of Eco-Chemical Engineering, Ministry of Education, State Laboratory of Inorganic Synthesis and Applied Chemistry, College of Chemistry and Molecular Engineering, Qingdao University of Science and Technology, Qingdao 266042, China

* Corresponding Authors: xujix47@163.com (J.X. Xu); inorchemwl@126.com (L. Wang)

Experimental section

Characterization

Powder X-ray diffraction (XRD) data were collected using a Rigaku D–MAX 2500/PC diffractometer equipped with a Cu Kα radiation source. X-ray photoelectron spectra (XPS) were recorded using an X-ray photoelectron spectrometer (Thermo Scientific, Kα) equipped with a monochromatic Al Ka X-ray source ($h\nu$ = 1486.6 eV). UV–visible diffuse reflectance spectra were recorded using a Lambda 750 UV/VIS/NIR spectrometer. The morphology of the samples was investigated by using scanning electron microscopy (SEM, SU8000) and transmission electron microscopy (TEM, JEM–ARM 200F, JEOL). Energy-dispersive X-ray (EDX) elemental mapping were recorded using a Bruker super-X energy-dispersive X-ray spectrometer. A Fluor-spectrophotometer (F-4500 FL) was used to record photoluminescence (PL) spectra. Fourier transform infrared (FTIR) spectra were recorded on a Nicolet 6700 spectrometer with KBr pellet (Thermo scientific, USA). O_2 adsorption on the catalysts was measured by temperature programmed desorption (TPD) using a chemisorption Analyzer (AutoChem II 2920, Micromeritics).

Electrochemical and photoelectrochemical measurements

The photocurrent measurements and electrochemical impedance spectroscopy (EIS) were recorded using a standard three-electrode electrochemical analyzer (PEC2000, Beijing). The sample coated onto an FTO electrode acts as the working electrode; a SCE (saturated calomel electrode) acts as the reference electrode; a Pt foil acts as the counter electrode. A 300-W Xe arc lamp (PLS-SXE300) was used as the light source.

A 0.5 M Na_2SO_4 aqueous solution was used as the electrolyte. The rotating disk electrode (RDE) measurements were performed on with an Ag/AgCl electrode and a Pt electrode as reference and counter electrode, respectively. The LSV curves were obtained in an O_2-saturated 0.1 M phosphate buffer solution. O_2 was kept flowing on the liquid surface of the electrolyte during testing. The average transfer electron number (*n*) in the overall O_2 reduction was obtained by the slopes of Koutecky–Levich plots with the following equation:

$$j^{-1} = j_k^{-1} + B^{-1}\Omega^{-1/2}$$

$$B = 0.2nF\nu^{-1/6}CD^{2/3}$$

where j, j_k, and Ω are the tested current density, kinetic current density, and rotating speed (rpm), respectively. F and v are the Faraday constant (96485 C mol^{-1}) and kinetic viscosity of water (0.01 cm^2 s^{-1}), C and D are the bulk concentration of O_2 in water (1.26×10^{-3} mol cm^{-3}) and the diffusion coefficient of O_2 (2.7×10^{-5} cm^2 s^{-1}).

Photocatalytic H_2O_2 production

10 mg of obtained photocatalyst was dispersed into 50 mL pure water. Then, oxygen was bubbled to achieve saturation adsorption. After that, the suspension was irradiated by a 300 W Xenon lamp equipped with a 420 nm cut off filter. 5 mL of suspension was withdrawn at each time interval and the concentration of produced H_2O_2 was determined by iodometry. To evaluate the recyclability of the photocatalyst, the sample was collected by centrifugation and washed with deionized water and dried before use in the next cycle experiments.

H_2O_2 decomposition tests

The H_2O_2 decomposition behavior was studied by dispersing 10 mg of catalyst in 50 mL of 1 mmol L^{-1} H_2O_2 solution and irradiating with visible light ($\lambda \geq 420$ nm) under continuous stirring. About 5 mL of the suspension was withdrawn at various time intervals and was then centrifuged to remove catalyst prior to determination of H_2O_2 concentration.

Measurement of H_2O_2 concentration

0.05 mL of 0.01 mol L^{-1} ammonium molybdate aqueous solution and 2 mL of 0.1 mol L^{-1} potassium iodide aqueous solution were added to 1 mL obtained solution, and kept for 30 min. The H_2O_2 molecules reacted with iodide anions (I^-) to produce triiodide anions (I_3^-). The amount of I_3^- was determined by means of UV–vis spectroscopy on the basis of the absorbance at 350 nm, from which the amount of H_2O_2 produced was estimated by the equation which given in Figure S1.

Apparent quantum yield calculation

$$AQY = \frac{Number\ of\ reacted\ electrons}{Number\ of\ incident\ photons} \times 100\%$$

$$= \frac{2 \times number\ of\ evolved\ H_2O_2\ molecules}{Number\ of\ incident\ photons} \times 100\%$$

$$= \frac{2 \times n_{H_2O_2}}{n_p} \times 100\%$$

$$= \frac{2 \times n_{H_2O_2}}{\frac{P \times t \times \lambda}{h \times c}} \times 100\%$$

In this equation, $n_{H_2O_2}$ and n_p is the number of H_2O_2 molecules and photons, respectively, P denotes the light power, determined by CEL-NP2000 power meter; t is the illumination time (3600 s); λ is the incident light wavelength (420 nm); h

represents the Planck constant (6.63×10^{-34} J·s); and c is the light speed (3.0×10^{8} $m \cdot s^{-1}$).

Method of DFT calculation

DFT calculations were performed in the Vienna ab initio simulation package (VASP). A spin-polarized GGA PBE functional, all-electron plane-wave basis sets with an energy cutoff of 520 eV, and a projector augmented wave (PAW) method were adopted. A (3 × 3 × 1) Monkhorst-Pack mesh was used for the Brillouin-zone integrations to be sampled. The conjugate gradient algorithm was used in the optimization. The convergence threshold was set $1*10^{-4}$ eV in total energy and 0.05 eV/ Å in force on each atom.

The adsorption energy change (ΔE_{abs}) was determined as follows:

$\Delta E_{abs} = E_{total} - E_{sur} - E_{mol}$

where E_{total} is the total energy for the adsorption state, E_{sur} is the energy of pure surface, E_{mol} is the energy of substrate.

Results Section

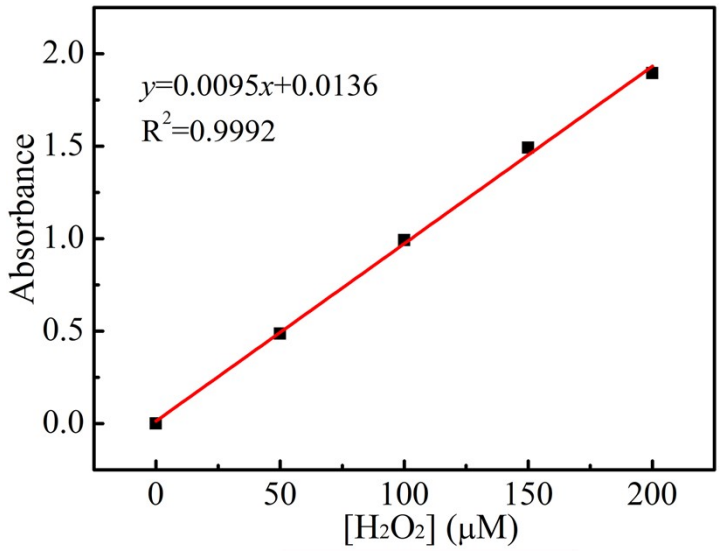

Fig. S1. The standard curve used for determination the concentration of H_2O_2.

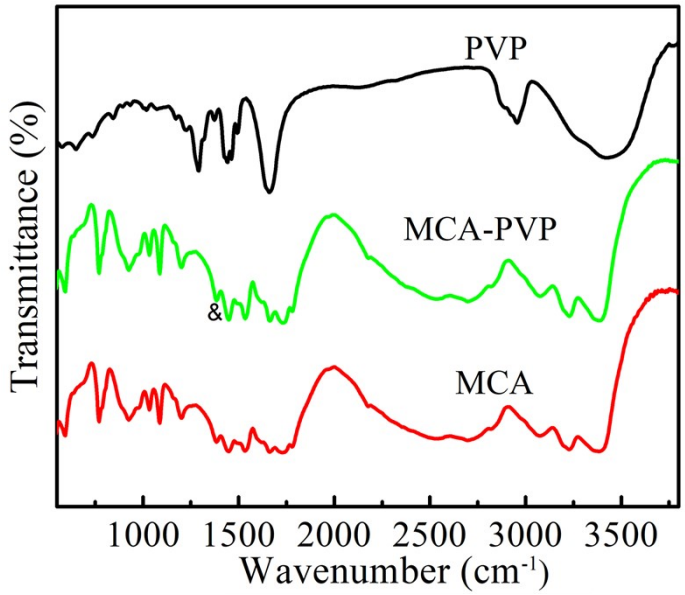

Fig. S2. FTIR spectra of PVP, MCA-PVP, and MCA samples.

Compared to FTIR spectrum of MCA, a new peak at 1400 cm^{-1} corresponding to bend vibration of CH_2 was observed. This indicates MCA was encapsulated by PVP.

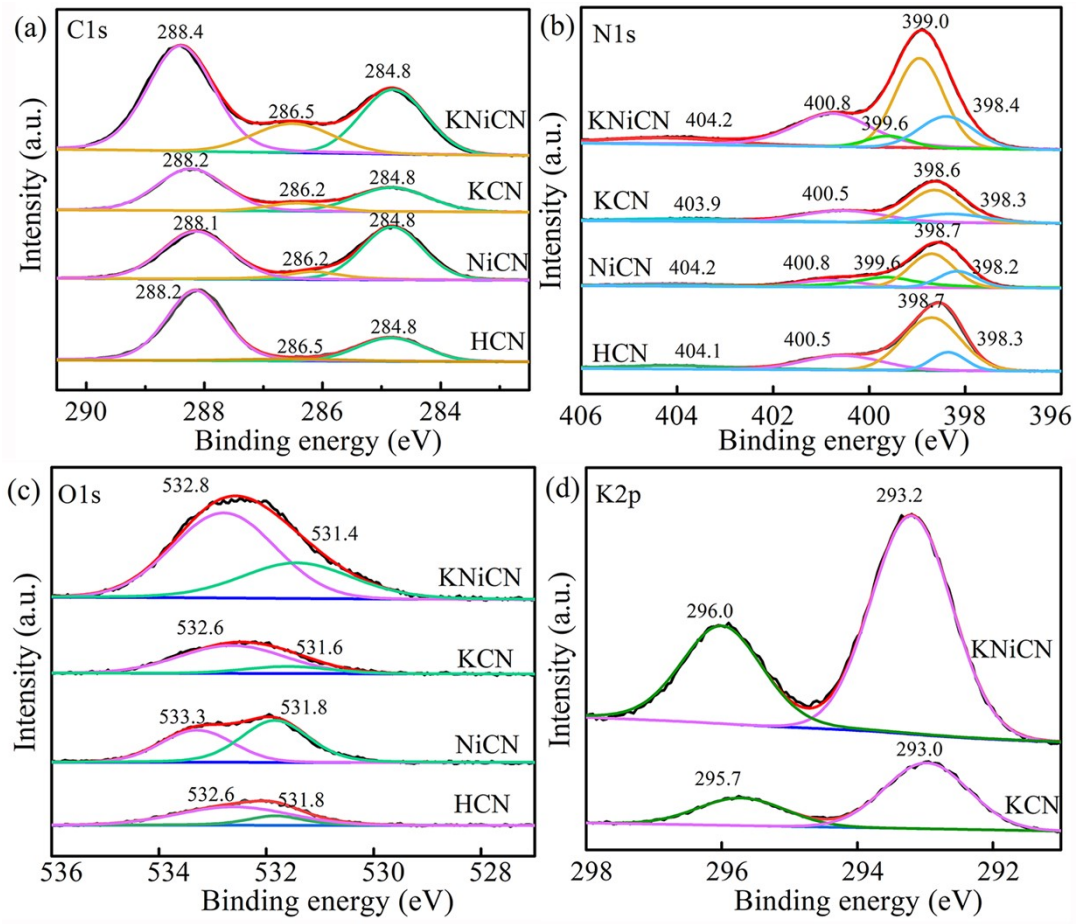

Fig. S3. High-resolution XPS spectra of (a) C1s, (b) N1s, (c) O1s, and (d) K2p of HCN, NiCN, KCN, and KNiCN samples.

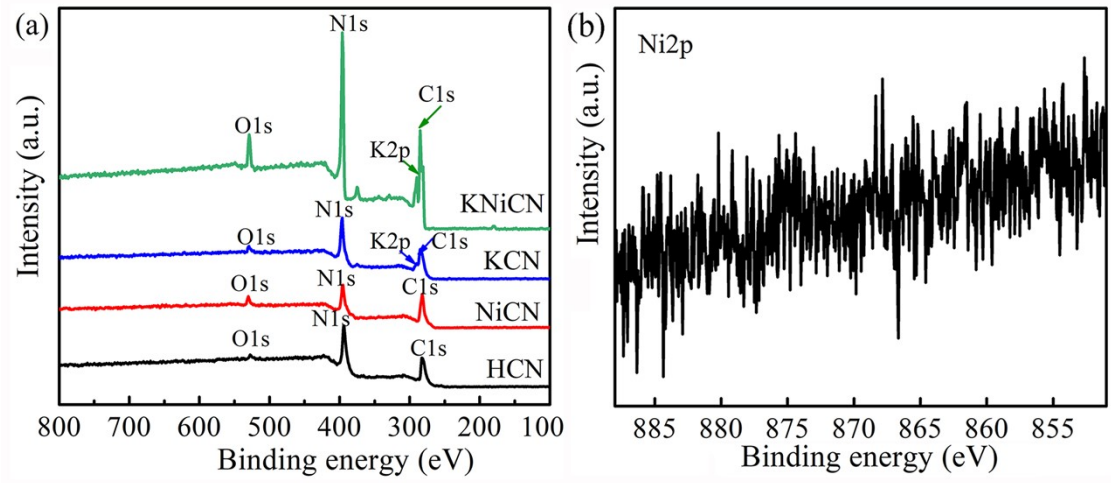

Fig. S4. (a) The survey XPS spectrum of obtained samples, (b) high-resolution XPS spectra of Ni2p in KNiCN.

The Ni2p peak could not be detected clearly in KNiCN owing to the low Ni content (24.2mg/kg_{KNiCN}, measured by ICP) on the catalysts surface and the limited analysis depth of XPS (10 nm). But the zeta potentials of KCN and KNiCN were measured. Values of –36 and –33.6 mV were obtained for KCN and KNiCN, respectively. The less negative charge of KNiCN suggests that the Ni bears a positive charge.

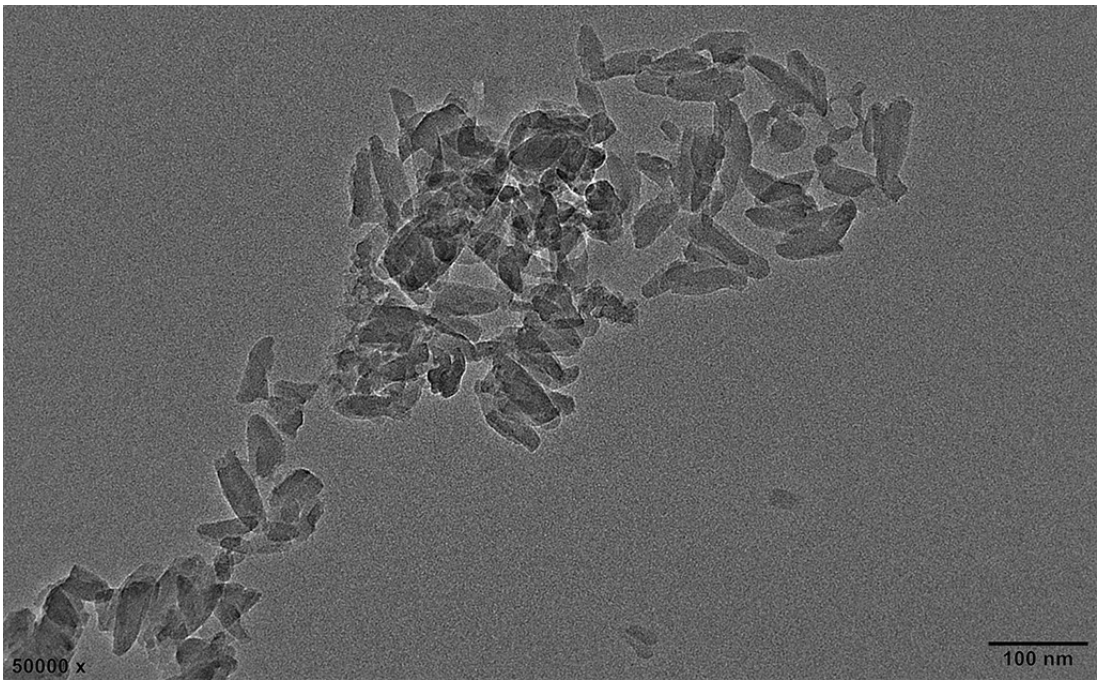

Fig. S5. TEM image of KCN.

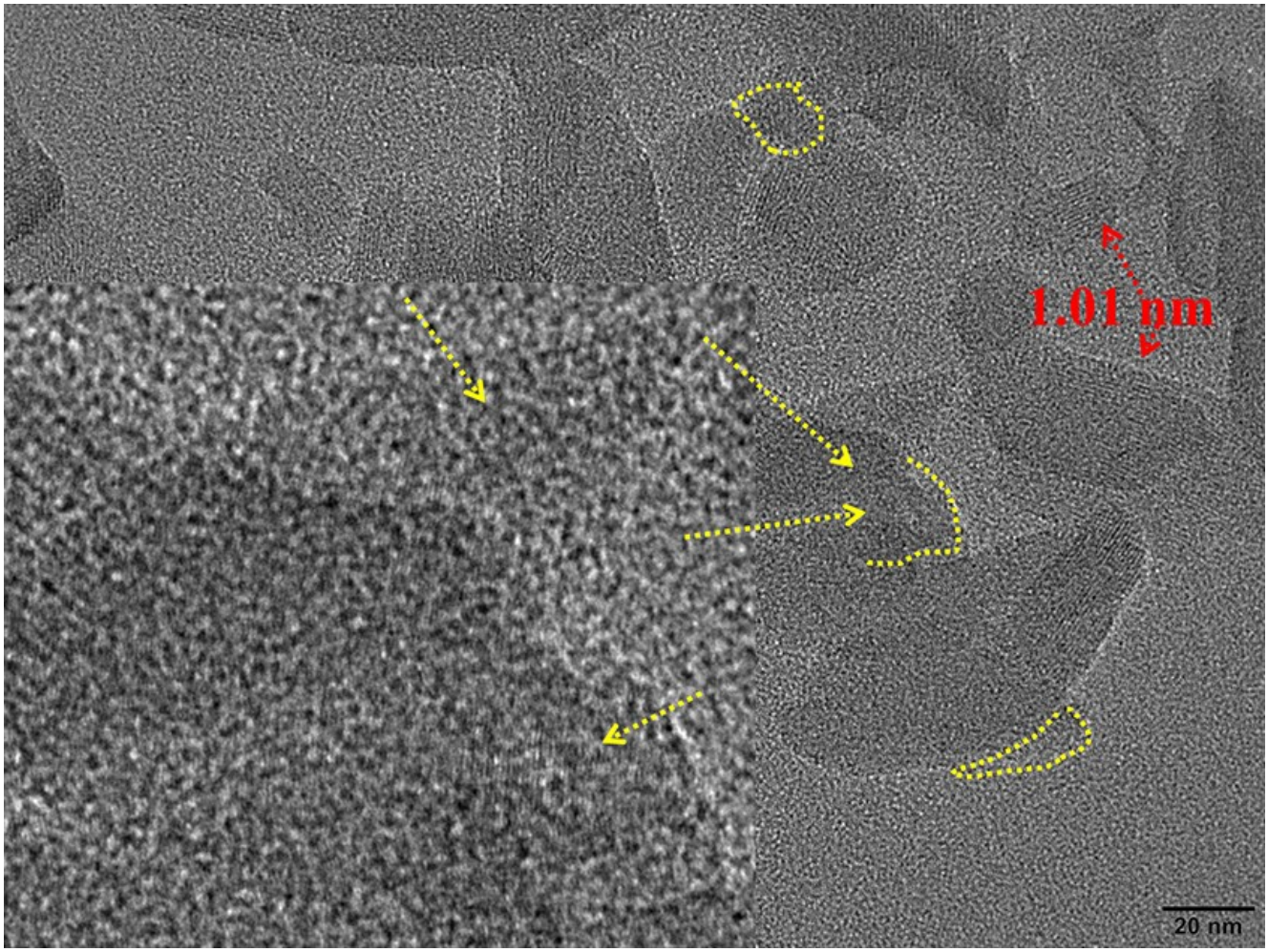

Fig. S6. HRTEM image of KNiCN (the inset is partial enlarged image).

KNiCN exhibits a lattice fringe with interlayer distances of 1.01 nm (red arrows), which was attributed to in-plane repeated units. In addition, a 0.21 nm lattice fringe was observed (inset), which was ascribed to the (100) planes of graphite (marked by arrows).

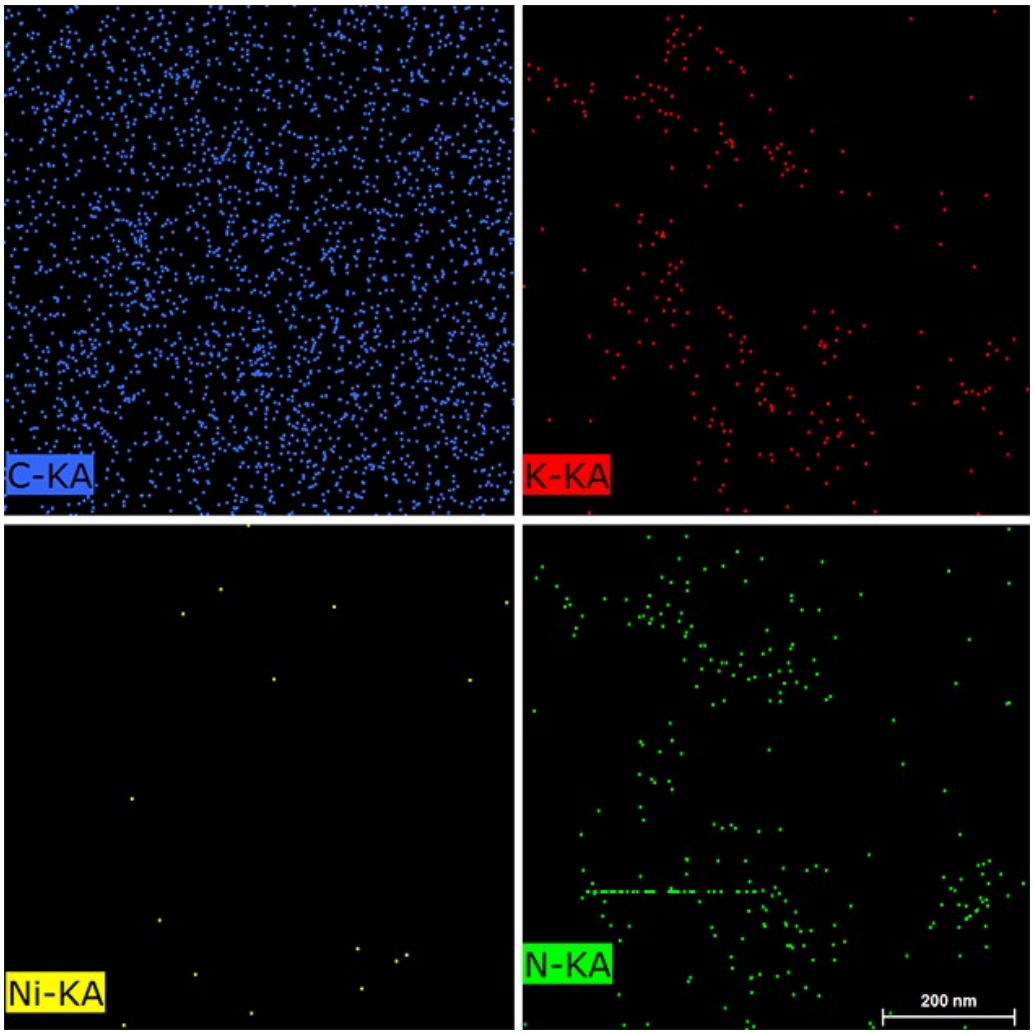

Fig. S7. EDX elemental mapping of C, N, Ni, and K of KNiCN sample.

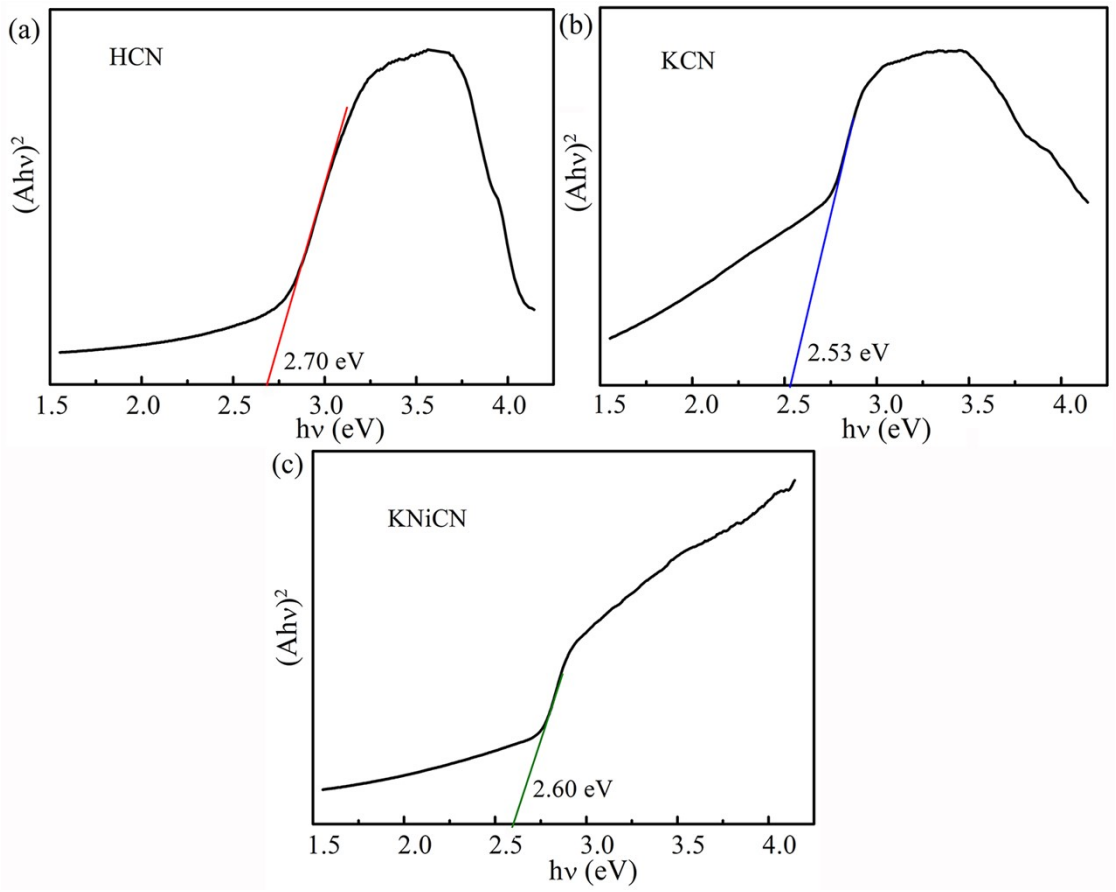

Fig. S8. Plots of transformed Kubelka–Munk function of HCN, KCN, and KNiCN.

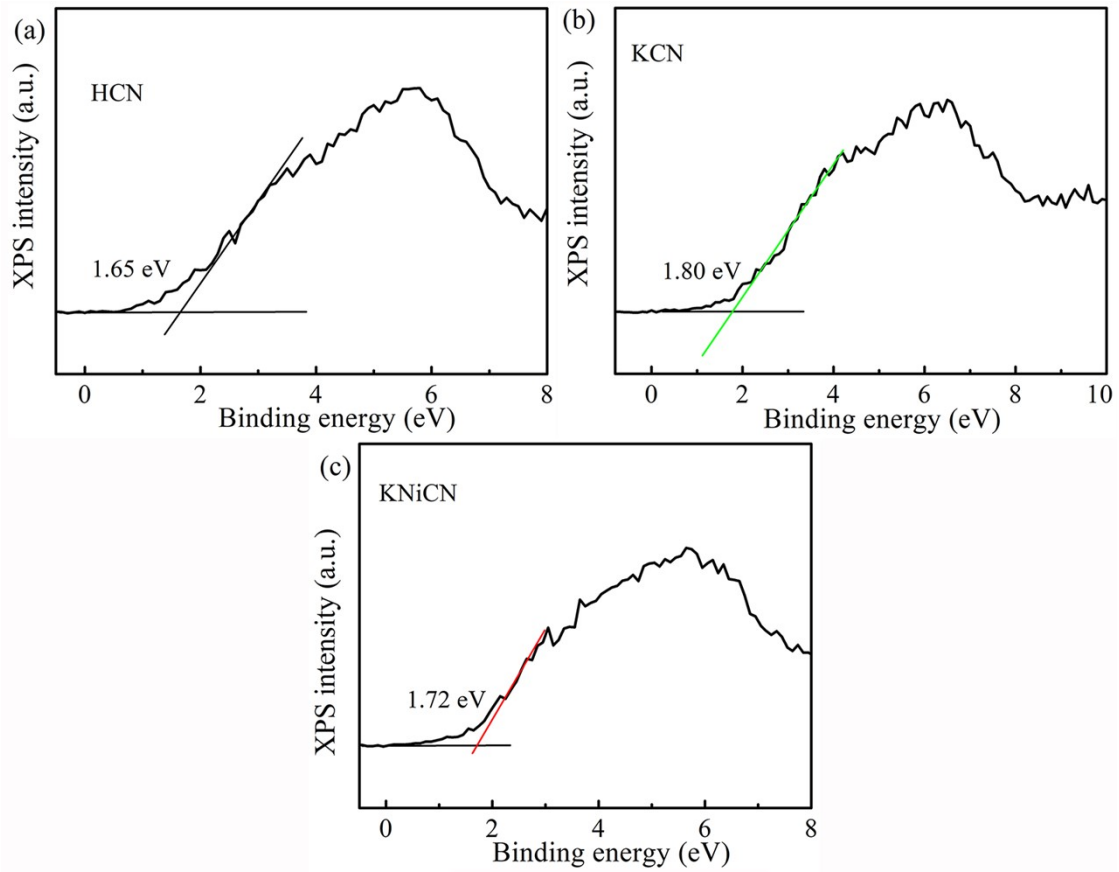

Fig. S9. XPS valence band spectra of HCN, KCN, and KNiCN.

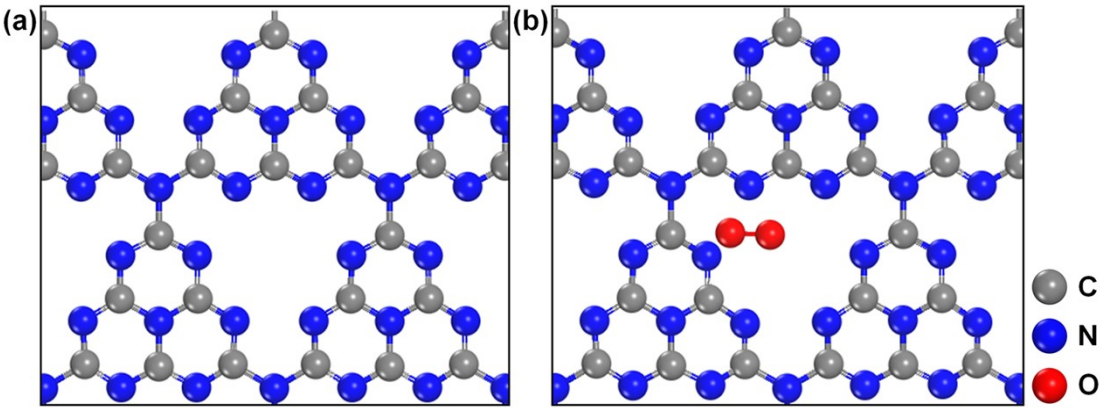

Fig. S10. The proposed structure of HCN (a) and O_2 adsorption sites in HCN (b).

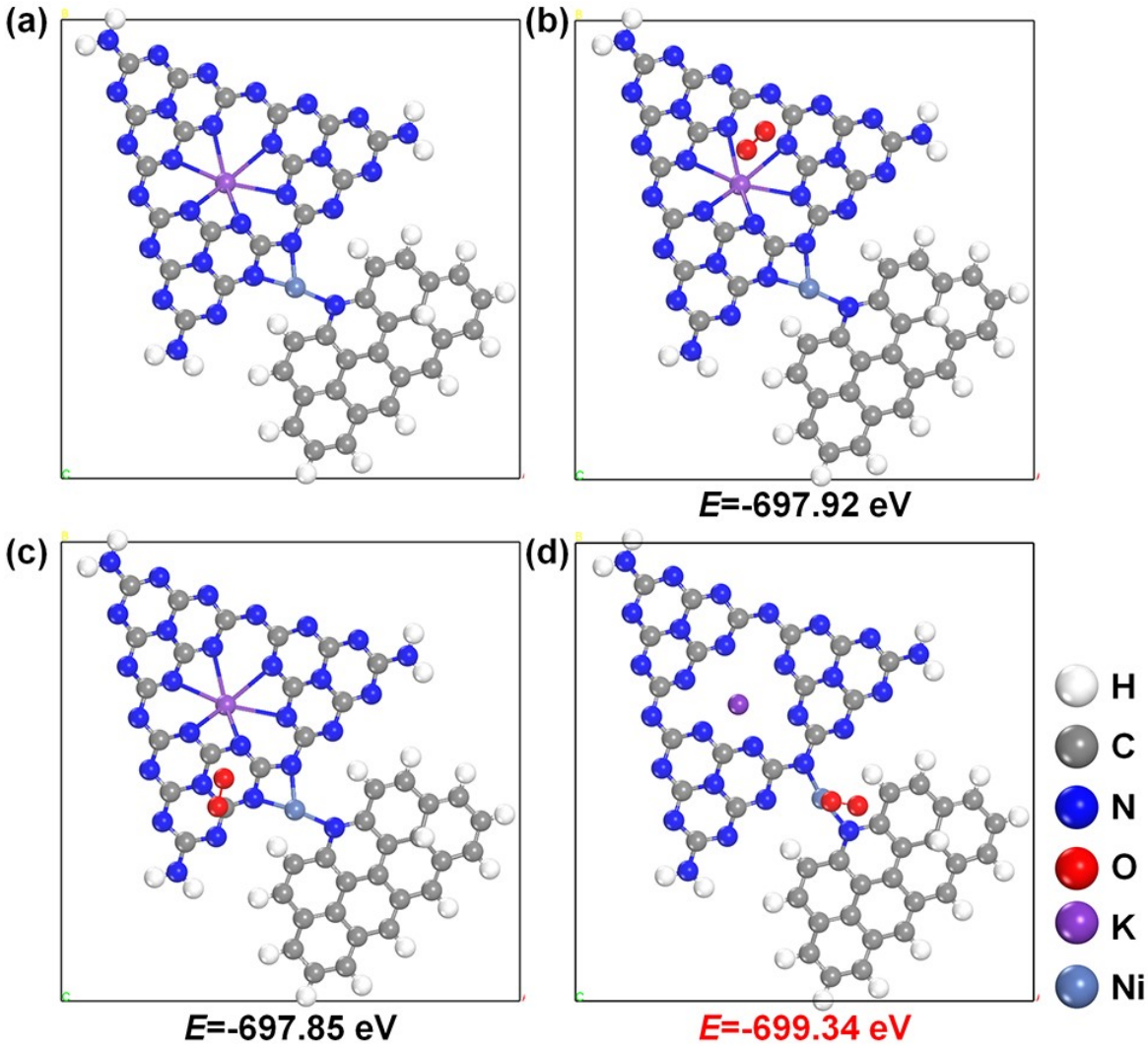

Fig. S11. The (a) proposed structure of KNiCN, (b-d) possible O_2 adsorption site in KNiCN sample.

A largest negative energy of –699.34 eV obtained with the structure of (d), where Ni was bonded with two N atoms coming from g-C_3N_4 and N-doped carbon. The O_2 molecules would prefer to adsorb on the Ni-N_2 sites.

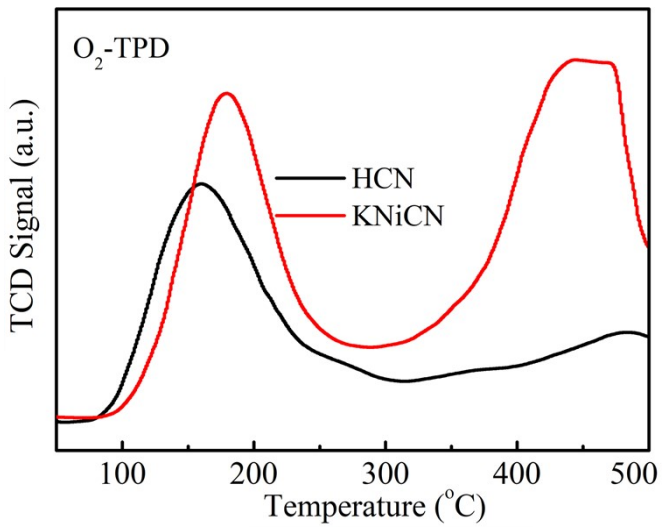

Fig. S12. MS signals of O_2 desorption for O_2-TPD profiles over samples of HCN and KNiCN.

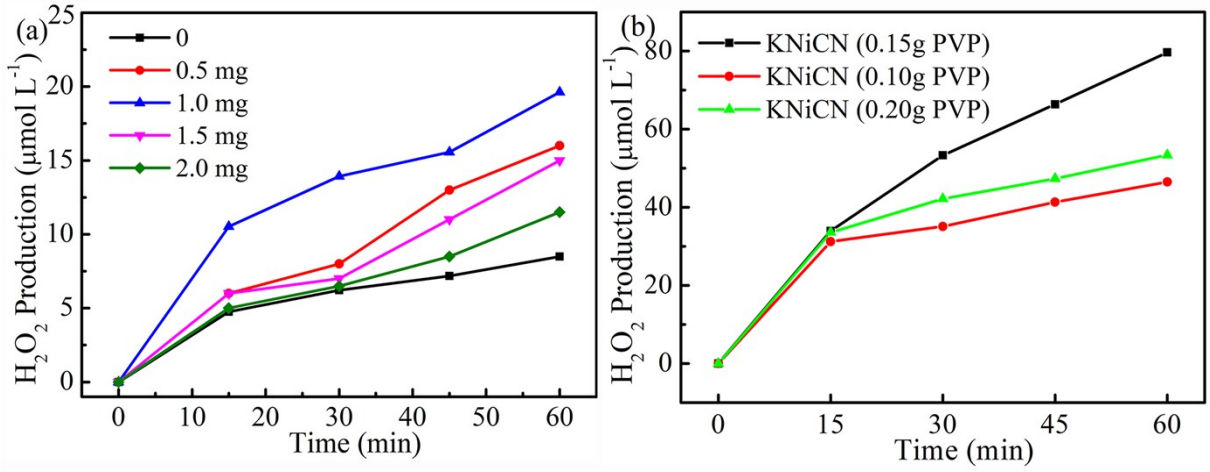

Fig. S13. Effect of (a) Ni^{2+} and (b) PVP amounts on H_2O_2 production.

Compared to HCN, all Ni modified CN exhibited better H_2O_2 production activity than HCN with NiCN prepared by calcination with PVP/MCA loaded with 1 mg Ni^{2+} generating optimal H_2O_2 yields of 19.6 μM. Moreover, when the mass ratio of PVP to MCA is 0.15 : 0.2, the obtained KNiCN shows the highest H_2O_2 production activity.

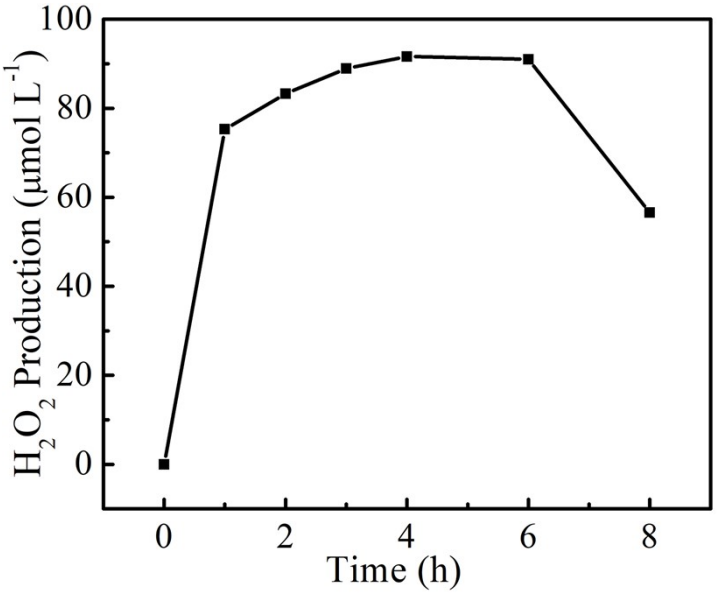

Fig. S14. The yield of H_2O_2 with time prolong over KNiCN.

A linear increment in the H_2O_2 concentration is observed for KNiCN up to a test run of 6 h, after which its concentration decreased, indicating that the H_2O_2 decomposition become serious.

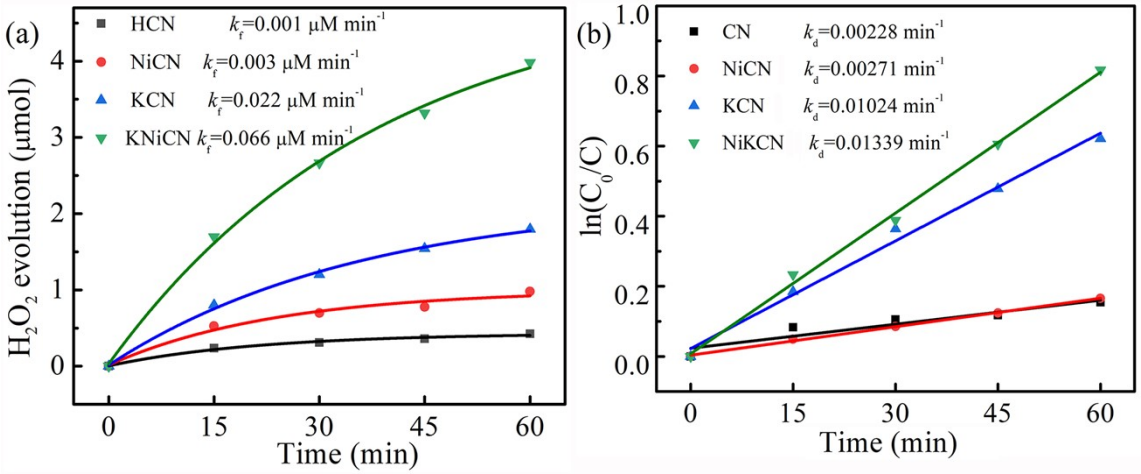

Fig. S15. (a) Zero-order and (b) pseudo-first-order kinetic curves of H_2O_2 formation and degradation, respectively over HCN, NiCN, KCN, and KNiCN.

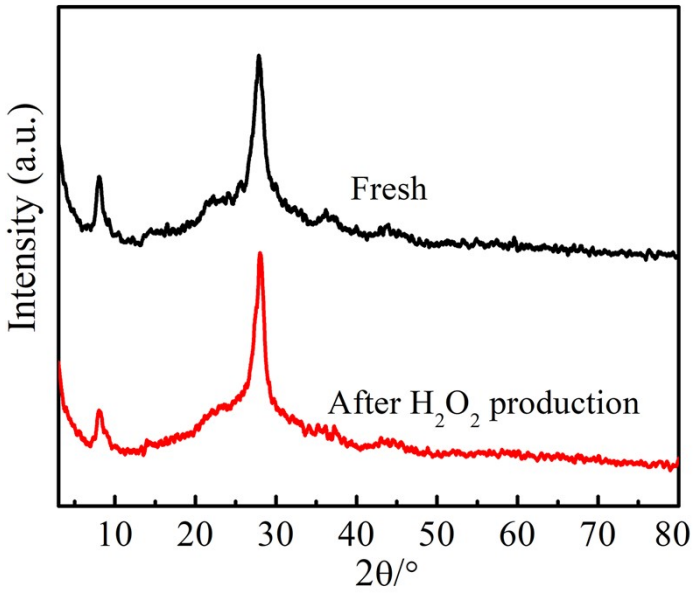

Fig. S16. XRD patterns of fresh and used KNiCN.

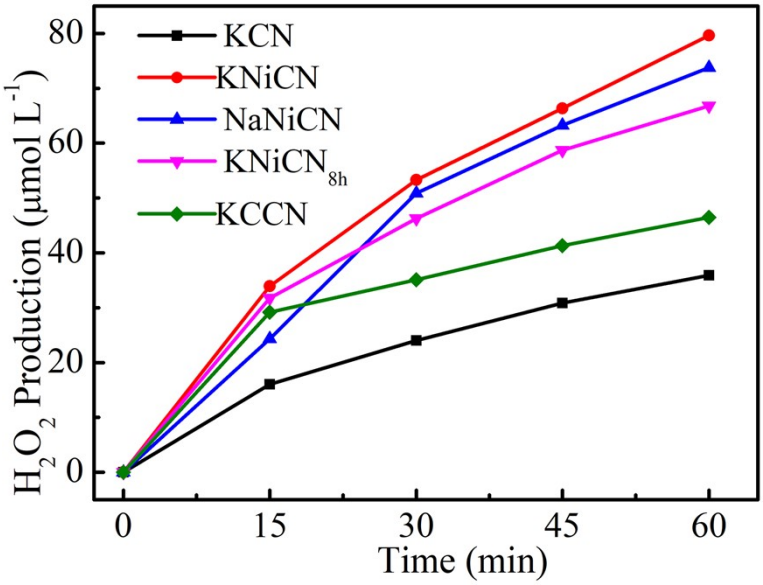

Fig. S17. Comparison H_2O_2 production performance of various samples.

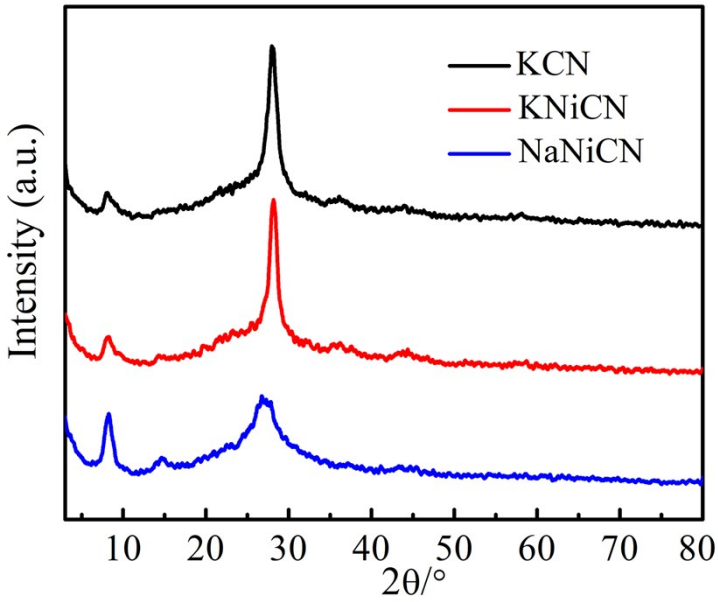

Fig. S18. XRD patterns of KCN, KNiCN, and NaNiCN.

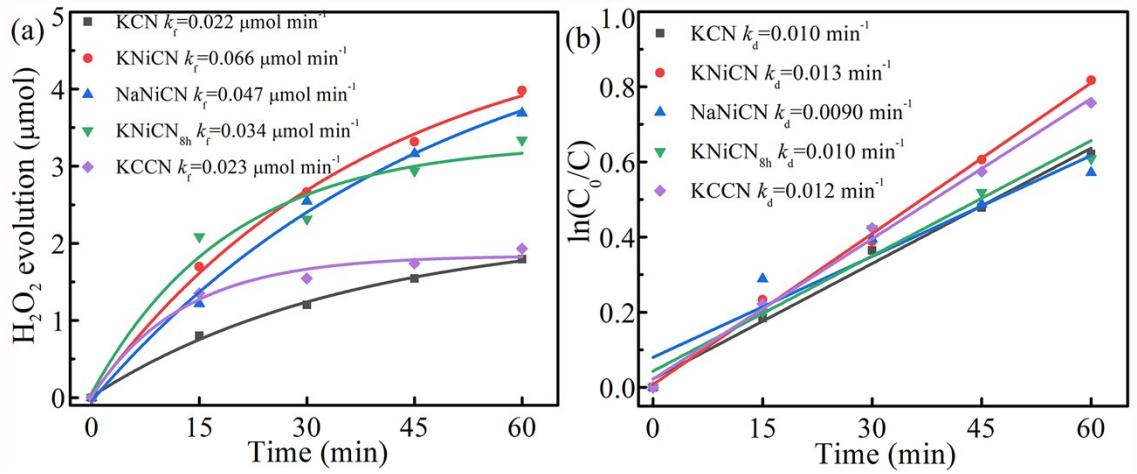

Fig. S19. (a) Zero-order and (b) pseudo-first-order kinetic curves of H_2O_2 formation and degradation, respectively of various samples.

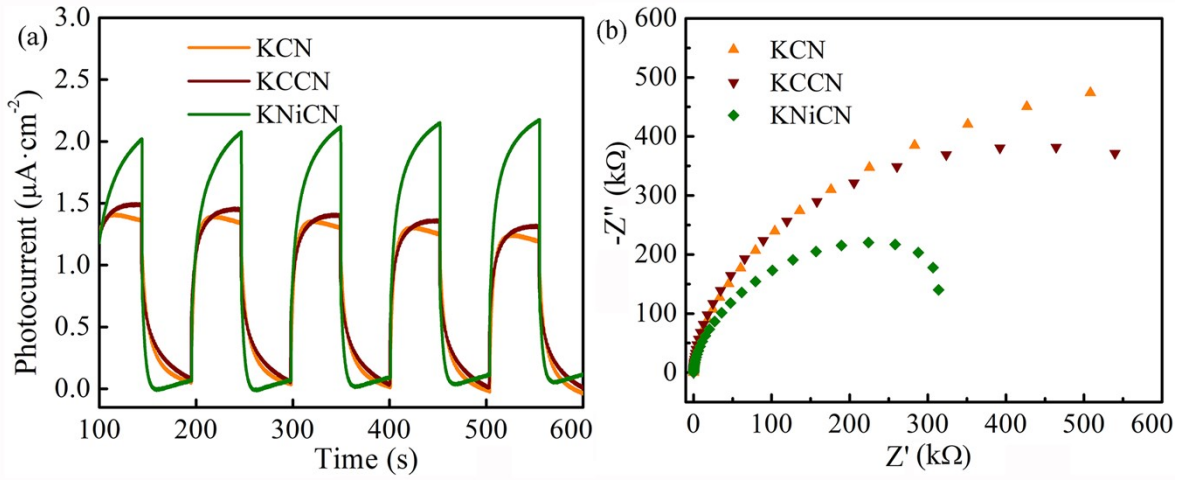

Fig. S20. (a) Transient photocurrent, (d) EIS results of KCN, KNiCN, and KCCN.

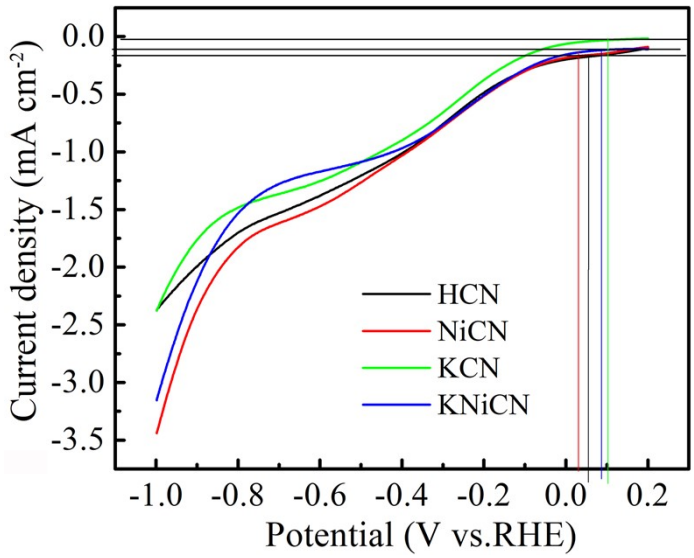

Fig. S21. Linear sweep voltammetry **(**LSV) curves of PCN, BCN, KCN, and KBCN measured on RDE at1600 rpm.

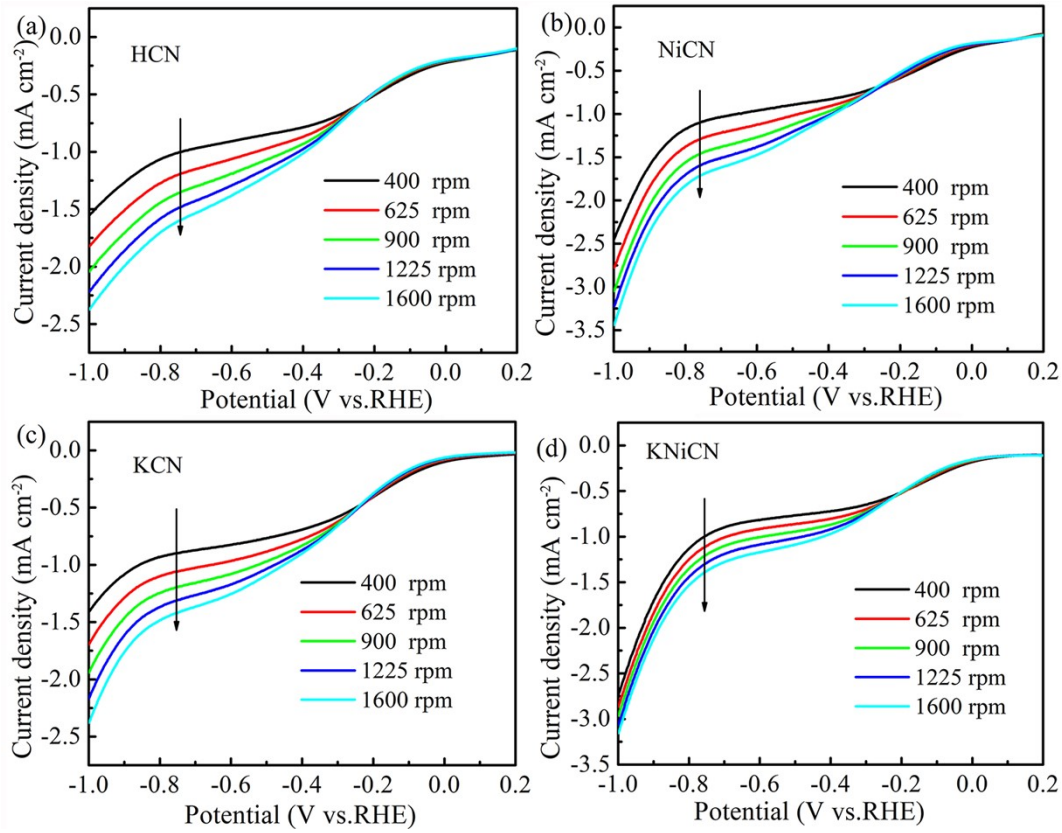

Fig. S22. LSV curves of HCN, NiCN, KCN, and KNiCN measured on RDE at different rotating speeds.

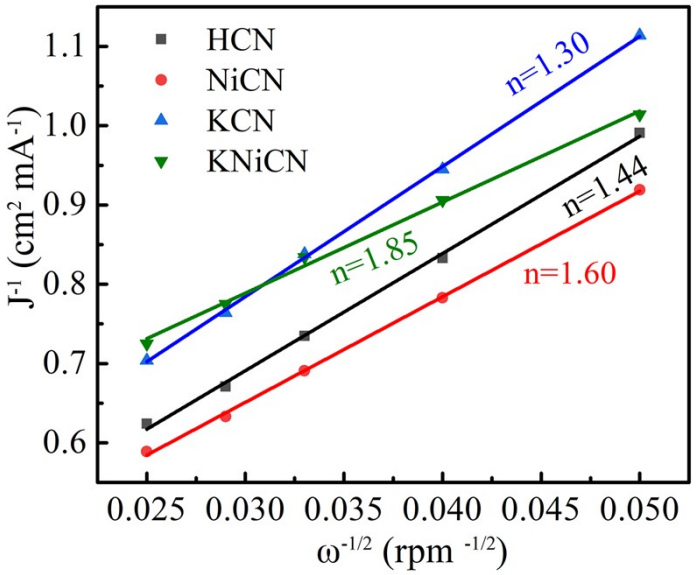

Fig. S23. The Koutecky–Levich plots of HCN, NiCN, KCN and KNiCN.

Table 1 Comparison photocatalytic H_2O_2 production of g-C_3N_4-based catalysts.

Photocatalysts	**H_2O_2 yield ($\mu mol \cdot g^{-1} \cdot h^{-1}$)**	**Light irradiation**	**Catalyst/ mg**	**H_2O/mL**	**Reference**
Ni-CAT-CN_{60}	1801	Xenon lamp, $\lambda \geq 420$ nm	10	15	[1]
AQ/U-POCN	150	300 W Xenon lamp, 400-780 nm	10	20	[2]
Co_1/AQ/ C_3N_4	124	AM1.5, simulated solar	6	12	[3]
g-C_3N_4/PDI-$rGO_{0.05}$	24.17	43.3 $W \cdot m^{-2}$ Xenon lamp, 420−500nm	50	30	[4]
R_{370}-CN	170	300 W Xenon lamp, $\lambda \geq 420$ nm	100	100	[5]
$PTA_{0.6}$/CN	833	Xenon lamp, 420-700 nm	10	15	[6]
ACNT-5	240.36	AM1.5, simulated solar	50	50	[7]
Cv-g-C_3N_4	92	300 W Xenon lamp, $\lambda \geq 420$ nm	100	100	[8]
3DOM g-C_3N_4-PW_{11}	35	300 W Xenon lamp, $\lambda > 320$ nm	100	100	[9]
g-C3N4/BDI_{50}	8.54	simulated solar, 420-500 nm	100	30	[10]
PCNBA-0.2	~2.4mg/L	AM1.5, 400-500 nm	50	30	[11]
PEI/C_3N_4	208.1	100mW·cm^{-2}, simulated solar	20	20	[12]
g-C_3N_4-CoWO	187.5	300 W Xenon lamp, $\lambda \geq 420$ nm	100	100	[13]
CPN	1968	Xenon lamp, 420-700 nm,	10	15	[14]
C-N-g-C_3N_4	49	40 mW·cm^{-2}, Xenon lamp, 420-700 nm	20	15	[15]
g-C_3N_4-PWO	62.5	300 W Xenon lamp, $\lambda \geq 420$ nm	100	100	[16]
KNiCN	398	300 W Xenon lamp, $\lambda \geq 420$ nm	10	50	This work

REREFENCES

[1] Y. J. Zhao, Y. Liu, Z. Z. Wang, Y. R. Ma, Y. J. Zhou, X. F. Shi, Q. Y. Wu, X. Wang, M. W. Shao, H. Huang, Y. Liu, Z. H. Kang, Carbon nitride assisted 2D conductive metal-organic frameworks composite photocatalyst for efficient visible light-driven H_2O_2 production, *Appl. Catal. B: Environ.*, 2021, **289**, 120035–120042.

[2] Y. X. Ye, C. Wen, J. H. Pan, J. W. Wang, Y. J. Tong, S. B. Wei, Z. F. Ke, L. Jiang, F. Zhu, N. B. Zhou, M. J. Zhou, J. Q. Xu, G. F. Ouyang, Visible-light driven efficient overall H_2O_2 production on modified graphitic carbon nitride under ambient conditions, *Appl. Catal. B: Environ.*, 2021, **285**, 119726–119733.

[3] C. Chu, Q. H. Zhu, Z. H. Pan, S. Gupta, D. H. Huang, Y. H. Du, S. Weon, Y. S. Wu, C. Muhich, E. Stavitski, K. Domen, J. H. Kim, Spatially separating redox centers on 2D carbon nitride with cobalt single atom for photocatalytic H_2O_2 production, *PNAS*, 2020, **117**, 6376–6382.

[4] Y. Kofuji, Y. Isobe, Y. Shiraishi, H. Sakamoto, S. Tanaka, S. Ichikawa, T. Hirai, Carbon nitride–aromatic diimide–graphene nanohybrids: metal-free photocatalysts for solar-to-hydrogen peroxide energy conversion with 0.2% efficiency, *J. Am. Chem. Soc.*, 2016, **138**, 10019–10025.

[5] Z. D. Zhu, H. H. Pan, M. Murugananthan, J. Y. Gong, Y. R. Zhang, Visible light-driven photocatalytically active g-C_3N_4 material for enhanced generation of H_2O_2, *Appl. Catal. B: Environ.*, 2018, **232**, 19–25.

[6] J. J. Cao, Q. Y. Wu, Y. J. Zhao, K. Q. Wei, Y. Li, X. Wang, F. Liao, H. Huang, M. W. Shao, Y. Liu, Z. H. Kang, In-situ photovoltage transients assisted catalytic study on H_2O_2 photoproduction over organic molecules modified carbon nitride photocatalyst, *Appl. Catal. B: Environ.*, 2020, **285**, 119817–119826.

[7] L. Zhou, J. Y. Lei, F. C. Wang, L. Z. Wang, M. R. Hoffmann, Y. D. Liu, S. I. In, J. L. Zhang, Carbon nitride nanotubes with in situ grafted hydroxyl groups for highly efficient spontaneous H_2O_2 production, *Appl. Catal. B: Environ.*, 2021, **288,** 119993–120001.

[8] S. N. Li, G. H. Dong, R. Hailili, L. P. Yang, Y. X. Li, F. Wang, Y. B. Zeng, C. Y. Wang, Effective photocatalytic H_2O_2 production under visible light irradiation at g-C_3N_4 modulated by carbon vacancies, *Appl. Catal. B: Environ.*, 2016, **190**, 26–35.

[9] S. Zhao, X. Zhao, H. Zhang, J. Li, Y. F. Zhu, Covalent combination of polyoxometalate and graphitic carbon nitride for light-driven hydrogen peroxide production, *Nano Energy*, 2017, **35**, 405–414.

[10] Y. Kofuji, S. Ohkita, Y. Shiraishi, H. Sakamoto, S. Tanaka, S. Ichikawa, T. Hirai, Graphitic carbon nitride doped with biphenyl diimide: efficient photocatalyst for hydrogen peroxide production from water and molecular oxygen by sunlight, *ACS Catal.*, 2016, **6**, 7021−7029.

[11] Z. Y. Teng, W. N. Cai, S. X. Liu, C. Y. Wang, Q. T. Zhang, C. L. Su, T. Ohno, Bandgap engineering of polymetric carbon nitride copolymerized by 2,5,8-triamino-tri-s-triazine (melem) and barbituric acid for efficient nonsacrificial

photocatalytic H_2O_2 production, *Appl. Catal. B: Environ.*, 2020, **271**, 118917–118928.

[12] X. K. Zeng, Y. Liu, Y. Kang, Q. Y. Li, Y. Xia, Y. L. Zhu, H. L. Hou, M. H. Uddin, T. R. Gengenbach, D. H. Xia, C. H. Sun, D. T. Mccarthy, A. Deletic, J. G. Yu, X. W. Zhang, Simultaneously tuning charge separation and oxygen reduction pathway on graphitic carbon nitride by polyethylenimine for boosted photocatalytic hydrogen peroxide production, *ACS Catal.*, 2020, **10**, 3697−3706.

[13] S. Zhao, X. Zhao, Insights into the role of singlet oxygen in the photocatalytic hydrogen peroxide production over polyoxometalates-derived metal oxides incorporated into graphitic carbon nitride framework, *Appl. Catal. B: Environ.*, 2019, **250**, 408–418.

[14] J. J. Cao, H. Wang, Y. J. Zhao, Y. Liu, Q. Y. Wu, H. Huang, M. W. Shao, Y. Liu, Z. H. Kang, Phosphorus-doped porous carbon nitride for efficient sole production of hydrogen peroxide via photocatalytic water splitting with a two-channel pathway, *J. Mater. Chem. A*, 2020, **8**, 3701–3707.

[15] Y. J. Fu, C. A. Liu, M. L. Zhang, C. Zhu, H. Li, H. B. Wang, Y. X. Song, H. Huang, Y. Liu, Z. H. Kang, Photocatalytic H_2O_2 and H_2 generation from living chlorella vulgaris and ccarbon micro particle comodified g-C_3N_4, *Adv. Energy Mater.*, 2018, **8**, 1802525–1802533.

[16] S. Zhao, X. Zhao, Polyoxometalates-derived metal oxides incorporated into graphitic carbon nitride framework for photocatalytic hydrogen peroxide production under visible light, *J. Catal.*, 2018, **366**, 98–106.